nature portfolio

https://doi.org/10.1038/s41893-022-00947-z

# Supplementary information

# Sea-level rise from land subsidence in major coastal cities

In the format provided by the authors and unedited

# Supplementary

Positive values refer to land uplift or drop in mean sea-level, and negative values refer to land subsidence or rise in mean sea-level throughout the Supplementary. We use the same convention in the main text. All captions are above the figures in the Supplementary.

## A. Variability of relative local land subsidence across cities

The histograms of relative local land subsidence derived from Interferometric Synthetic Aperture Radar (InSAR) data for all 48 analyzed coastal cities are shown in this section (Fig. 1) and extend upon Fig. 1 in the main text. We also plot published rates of other components of relative sea-level rise (RSLR) for reference of their expected range of values across coastal cities (Fig. 1). These include the median of the coastal city's:

1. Climate-driven regional mean sea-level rise from the Intergovernmental Panel on Climate Change Sixth Assessment Report (IPCC AR6)[1–3] (see Supplementary C).
2. Vertical land motion (VLM) from IPCC AR6[1–3] (see "Reference to vertical land motion rates" in the main text).
3. Glacial isostatic adjustment contribution to VLM from the ICE-6G_C (VM5a) model[4,5] (see "Reference to glacial isostatic adjustment rates" in the main text).

Fig. 1: Histograms of the normalized number of pixels associated with each range of InSAR velocities within the administrative boundaries of coastal cities show that higher peak velocities coincide with higher proportions of subsiding areas. Peak velocity refers to the 95$^{th}$ percentile of negative InSAR velocities within the administrative boundary of a coastal city and are indicated by solid lines and upper-left numbers. Other components of relative sea-level rise are indicated by dashed lines for reference of their variabilities across different cities.

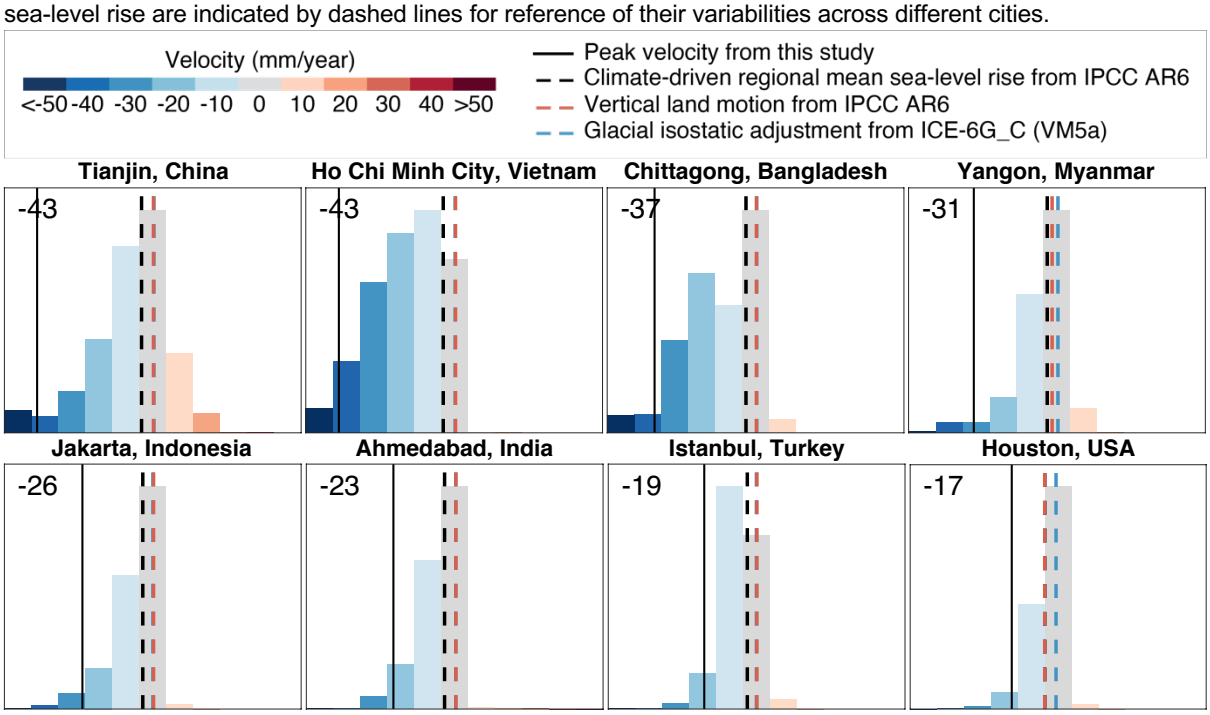

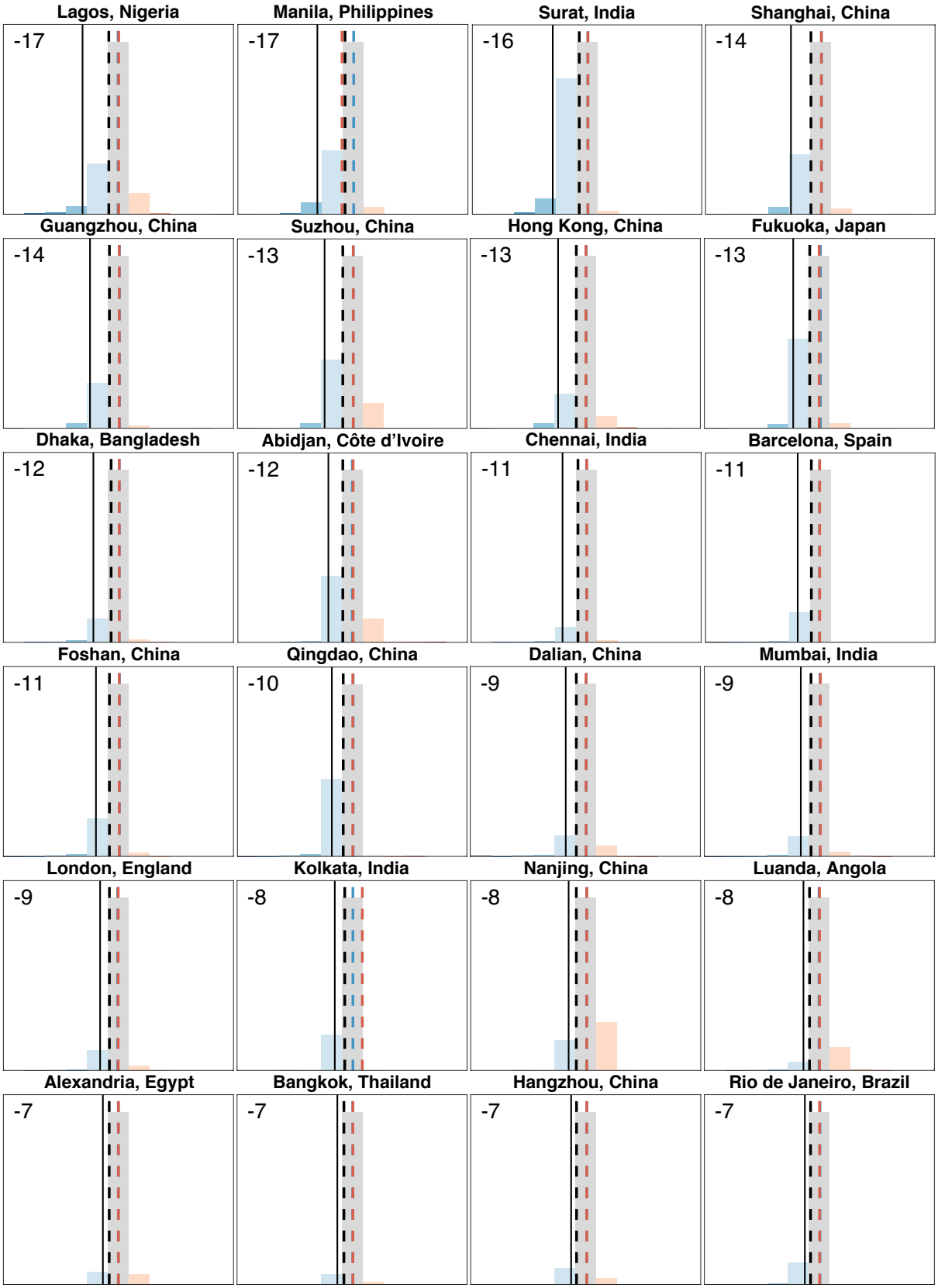
Lagos, Nigeria
-17
Manila, Philippines
-17
Surat, India
-16
Shanghai, China
-14
Guangzhou, China
-14
Suzhou, China
-13
Hong Kong, China
-13
Fukuoka, Japan
-13
Dhaka, Bangladesh
-12
Abidjan, Côte d'Ivoire
-12
Chennai, India
-11
Barcelona, Spain
-11
Foshan, China
-11
Qingdao, China
-10
Dalian, China
-9
Mumbai, India
-9
London, England
-9
Kolkata, India
-8
Nanjing, China
-8
Luanda, Angola
-8
Alexandria, Egypt
-7
Bangkok, Thailand
-7
Hangzhou, China
-7
Rio de Janeiro, Brazil
-7


Singapore, Singapore
-7
Karachi, Pakistan
-6
Osaka, Japan
-6
Saint Petersburg, Russia
-6
Dongguan, China
-5
Dar es Salaam, Tanzania
-5
Los Angeles, USA
-5
Miami, USA
-5
Lima, Peru
-4
Philadelphia, USA
-4
New York, USA
-4
Buenos Aires, Argentina
-4
Seoul, South Korea
-3
Tokyo, Japan
-3
Washington, D.C., USA
-3
Nagoya, Japan
-2

## B. Variability of relative local land subsidence within cities

The relative local land subsidence velocities for all 48 coastal cities are shown in this section (Fig. 2, 3). The velocities in each coastal city are relative to a selected reference point (see "InSAR time series processing" in the main text) and are not tied to a stable reference frame. The velocities may thus be shifted uniformly up or down if the entire city is uplifting or subsiding due to large-scale or region-wide processes.

We plot point measurements of VLM recorded by Global Navigation Satellite System (GNSS)[6] alongside our velocities to provide guidance on how our velocities may differ if tied to a stable reference frame. The GNSS data are obtained from Shirzaei et al.[6], tied to the IGS14 reference frame, and available in 25 of 48 coastal cities (Fig. 2). It should be noted that the InSAR and GNSS velocities should not be compared directly as the two instruments are sensitive to different types of land motion and need to be reconciled. InSAR detects the average elevation change of multiple scatterers within a pixel (90 m x 90 m in this study), while GNSS detects a single point. InSAR may also be sensitive to shallow subsurface changes such as the swelling of wet soils, while GNSS may be influenced by the depth which the monument is drilled into the ground and less likely to detect shallow subsurface changes. The InSAR data were measured between 2014 and 2020, while each GNSS record spans between 1 and 26 years. Nonetheless, GNSS may still be useful for adjusting the relative InSAR velocities to a stable reference frame if there is sufficient contextual knowledge of ongoing VLM processes in a coastal city.

Fig. 2: Relative local land subsidence in all analyzed coastal cities which contain at least one GNSS record overlapping an InSAR pixel in alphabetical order. GNSS data are obtained from Shirzaei et al.[6]. Basemap: ESRI.

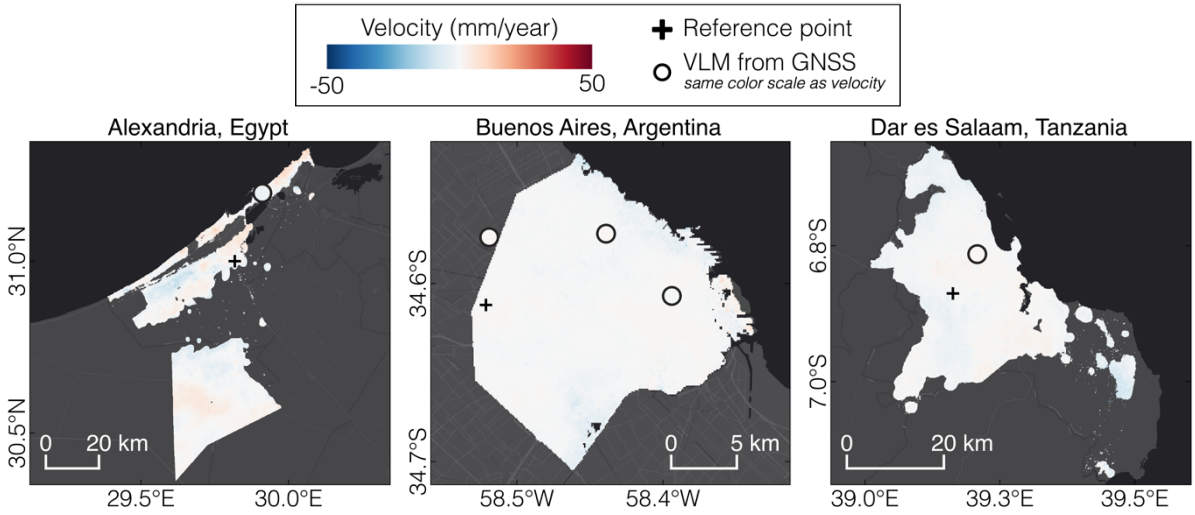

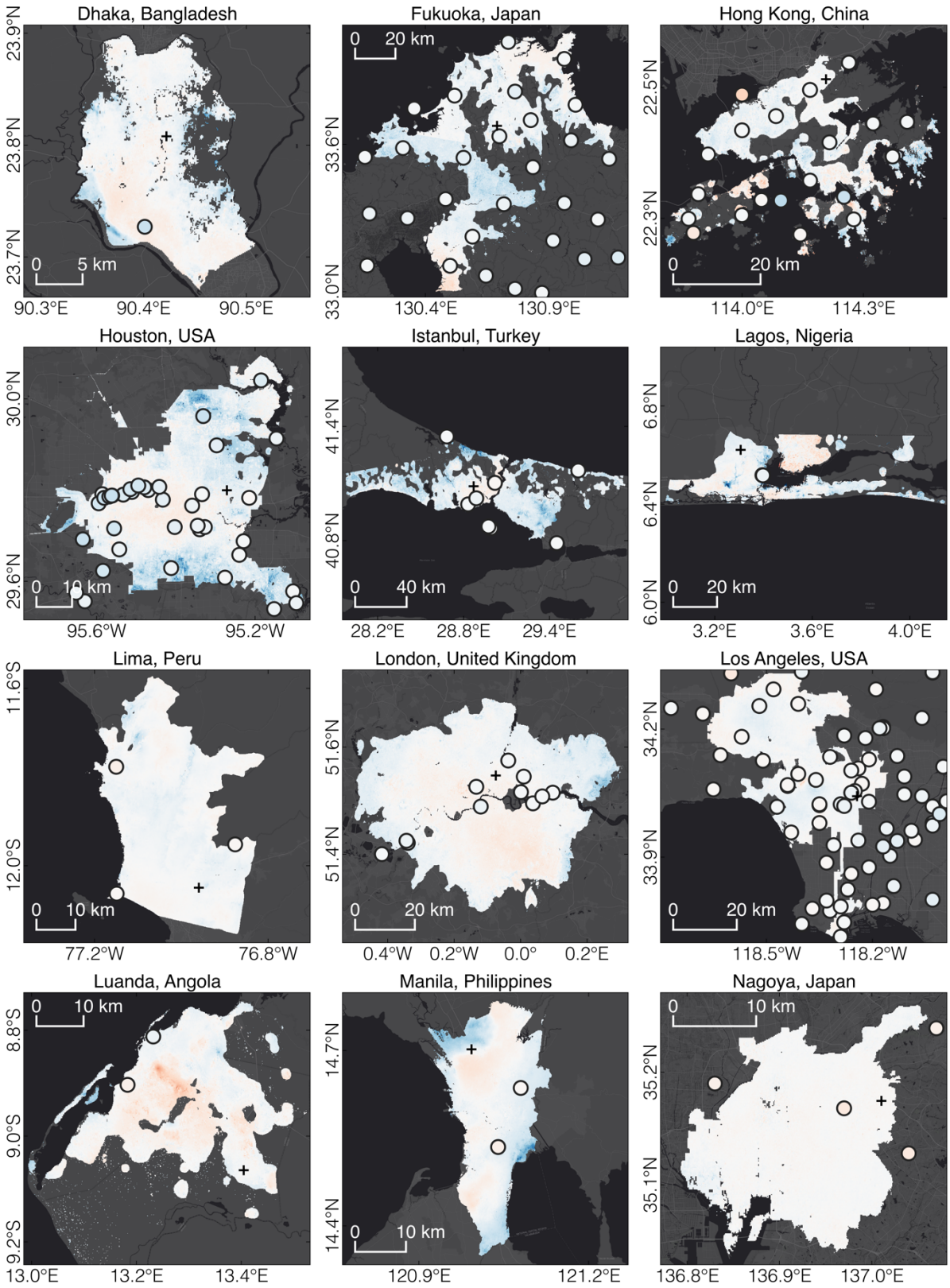
Dhaka, Bangladesh
23.9°N
23.8°N
23.7°N
0 5 km
90.3°E
90.4°E
90.5°E
Fukuoka, Japan
0 20 km
33.6°N
33.0°N
130.4°E
130.9°E
Hong Kong, China
22.5°N
22.3°N
0 20 km
114.0°E
114.3°E
Houston, USA
30.0°N
29.6°N
0 10 km
95.6°W
95.2°W
Istanbul, Turkey
41.4°N
40.8°N
0 40 km
28.2°E
28.8°E
29.4°E
Lagos, Nigeria
6.8°N
6.4°N
6.0°N
0 20 km
3.2°E
3.6°E
4.0°E
Lima, Peru
11.6°S
12.0°S
0 10 km
77.2°W
76.8°W
London, United Kingdom
51.6°N
51.4°N
0 20 km
0.4°W
0.2°W
0.0°
0.2°E
Los Angeles, USA
34.2°N
33.9°N
0 20 km
118.5°W
118.2°W
Luanda, Angola
0 10 km
8.8°S
9.0°S
9.2°S
13.0°E
13.2°E
13.4°E
Manila, Philippines
14.7°N
14.4°N
0 10 km
120.9°E
121.2°E
Nagoya, Japan
0 10 km
35.2°N
35.1°N
136.8°E
136.9°E
137.0°E

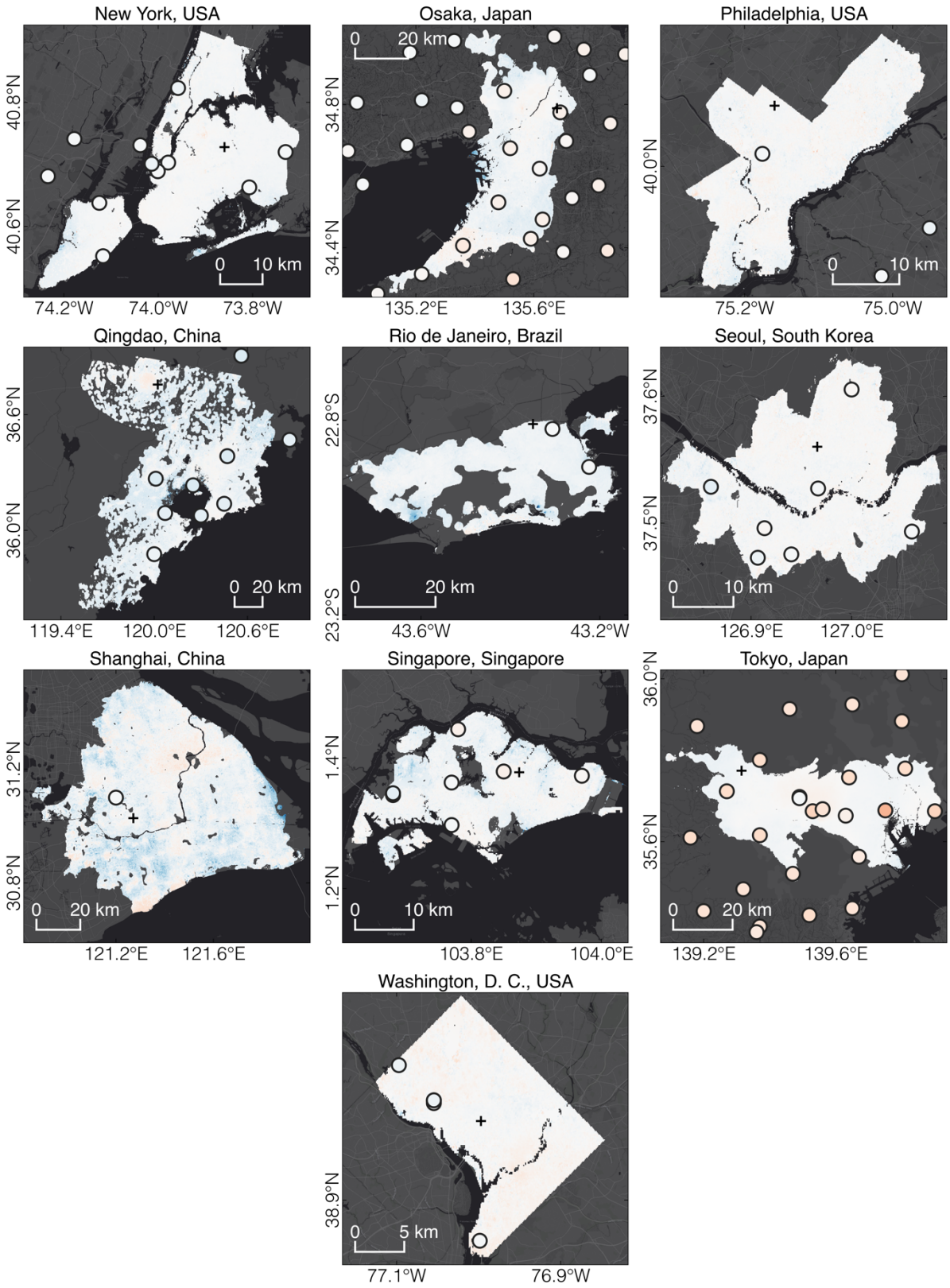
New York, USA
40.8°N
40.6°N
0 10 km
74.2°W
74.0°W
73.8°W
Osaka, Japan
0 20 km
34.8°N
34.4°N
135.2°E
135.6°E
Philadelphia, USA
40.0°N
0 10 km
75.2°W
75.0°W
Qingdao, China
36.6°N
36.0°N
0 20 km
119.4°E
120.0°E
120.6°E
Rio de Janeiro, Brazil
22.8°S
23.2°S
0 20 km
43.6°W
43.2°W
Seoul, South Korea
37.6°N
37.5°N
0 10 km
126.9°E
127.0°E
Shanghai, China
31.2°N
30.8°N
0 20 km
121.2°E
121.6°E
Singapore, Singapore
1.4°N
1.2°N
0 10 km
103.8°E
104.0°E
Tokyo, Japan
36.0°N
35.6°N
0 20 km
139.2°E
139.6°E
Washington, D. C., USA
38.9°N
0 5 km
77.1°W
76.9°W

Fig. 3: Relative local land subsidence in all analyzed coastal cities which do not have GNSS records within any single InSAR pixel in alphabetical order. Note that GNSS records shown below only appear to, but do not overlap any analyzed InSAR pixels due to the exaggerated size used to plot GNSS point measurements. GNSS data are obtained from Shirzaei et al.[6]. Basemap: ESRI.

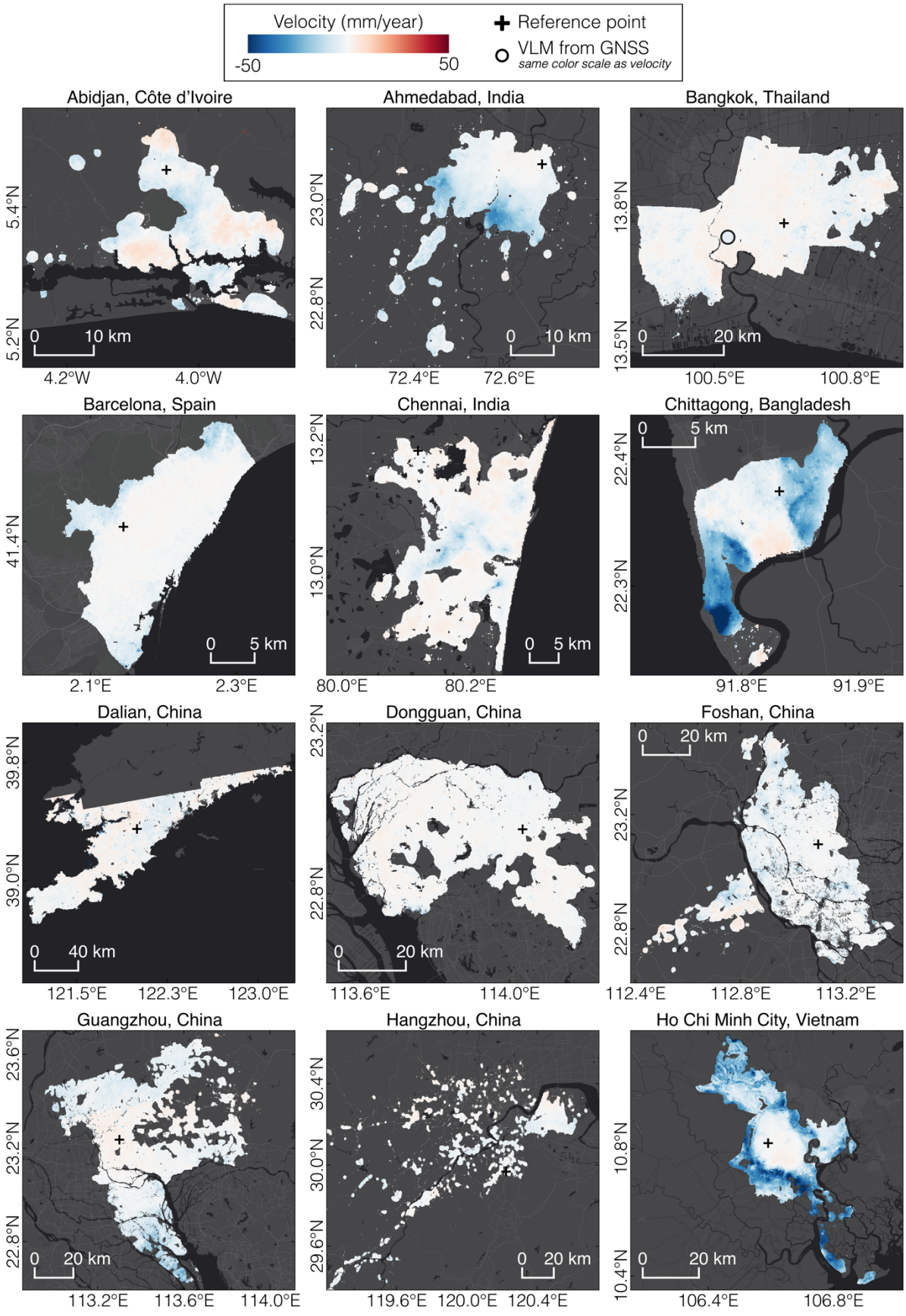

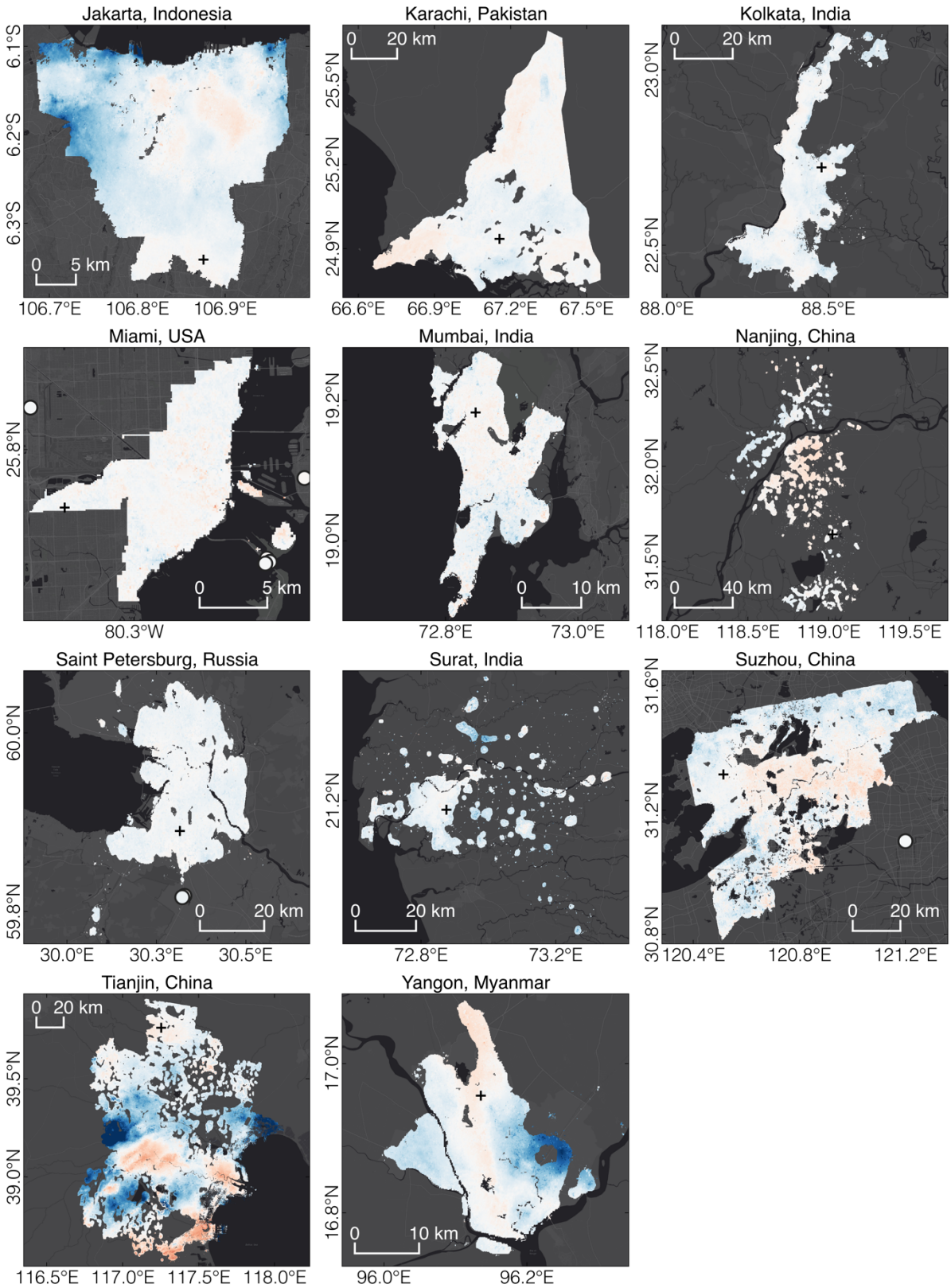
Jakarta, Indonesia
6.1°S
6.2°S
6.3°S
0 5 km
106.7°E 106.8°E 106.9°E
Karachi, Pakistan
0 20 km
25.5°N
25.2°N
24.9°N
66.6°E 66.9°E 67.2°E 67.5°E
Kolkata, India
0 20 km
23.0°N
22.5°N
88.0°E 88.5°E
Miami, USA
25.8°N
0 5 km
80.3°W
Mumbai, India
19.2°N
19.0°N
0 10 km
72.8°E 73.0°E
Nanjing, China
32.5°N
32.0°N
31.5°N
0 40 km
118.0°E 118.5°E 119.0°E 119.5°E
Saint Petersburg, Russia
60.0°N
59.8°N
0 20 km
30.0°E 30.3°E 30.5°E
Surat, India
21.2°N
0 20 km
72.8°E 73.2°E
Suzhou, China
31.6°N
31.2°N
30.8°N
0 20 km
120.4°E 120.8°E 121.2°E
Tianjin, China
0 20 km
39.5°N
39.0°N
116.5°E 117.0°E 117.5°E 118.0°E
Yangon, Myanmar
17.0°N
16.8°N
0 10 km
96.0°E 96.2°E

## C. Potential applications of relative local land subsidence

To illustrate examples of the potential application of the relative local land subsidence dataset to short-term RSLR assessments, we estimate the extent of inundation in selected coastal cities by 2030 using bathtub models (Fig. 4). We select two coastal cities, Ho Chi Minh City (Vietnam) and Rio de Janeiro (Brazil), where information on their regional VLM is available. The bathtub models account for local topography, climate-driven regional mean sea-level rise, and different components of VLM including relative local land subsidence. We obtain information for the bathtub models as follows:

1. Local topography: We use CoastalDEM[7] which has a reference year of 2000 and pixel spacing of 90 m. CoastalDEM is based on the globally available NASA Shuttle Radar Topography Mission Global 1 arc second Version 3.0 Digital Elevation Model[8], but has corrections applied over vegetation and densely populated areas to follow the height of the bare ground instead of the height of objects such as tall buildings standing on bare ground. CoastalDEM is thus suited for estimating inundation due to RSLR. We do not consider uncertainties in local topography in the bathtub model.
2. Climate-driven regional mean sea-level rise: We refer to projections for 2030 from the IPCC AR6 dataset[1–3] (https://podaac.jpl.nasa.gov/announcements/2021-08-09-Sea-level-projections-from-the-IPCC-6th-Assessment-Report). The dataset contains NetCDF files of projected rates of different RSLR components, at different percentile levels, under different Shared Socioeconomic Pathway (SSP) scenarios, in different years, and at irregular points that are mostly spaced 1 degree apart across the globe. The RSLR components include VLM values with no distinction between different VLM contributions and mean sea-level values due to Antarctic and Greenland ice sheets, glaciers, land water storage, and ocean dynamics. Projections are relative to a 1995 to 2014 baseline. Within this dataset, we refer to the medium confidence, SSP2-4.5 scenario as we consider SSP2-4.5 the most likely scenario where current climate policies remain in place, and projected emissions are neither particularly low nor high as in other SSP scenarios, but within Nationally Determined Contribution levels[1]. We sum the 50$^{th}$ percentile values of all RSLR components except for VLM, which is the only non-mean sea-level rise contribution. We only use data points over the ocean that are within a 1-degree radial distance from Ho Chi Minh City's and Rio de Janeiro's administrative boundaries and take the median to obtain one mean sea-level rise value per city. To compute the lower and upper limits of the bathtub model, we use the 16$^{th}$ and 84$^{th}$ percentile values instead of the 50$^{th}$ percentile values.
3. Relative local land subsidence component of VLM: We use velocities derived in this study and assume steady-state rates up to 2030. In using steady-state velocities, we assume no changes over the short-term in population, usage and policies of groundwater, oil, and gas extraction, and rates and spatial distributions of relative local land subsidence. It should be noted that this steady-state projection only serves to illustrate the potential effects of relative local land subsidence, where the underlying socio-economic conditions and extraction rates remain unchanged. A more accurate model of future extraction rates may be derived through future work. We also use the corresponding one standard deviation of the velocities at each pixel to compute the lower and upper limits of the bathtub model.
4. Glacial isostatic adjustment component of VLM: We use present-day rates from the ICE-6G_C (VM5a) model following the same method explained in "Reference to glacial

isostatic adjustment rates" of the main text. We use steady-state rates up to 2030 as glacial isostatic adjustment is a long-term process which continues at similar rates over thousands of years. We also use the corresponding one standard deviation of the ICE-6G_C (VM5a) rates derived by Li et al.[9] to compute the lower and upper limits of the bathtub model. The standard deviations are in a similar format as the ICE-6G_C (VM5a) rates and obtained for each city using the same method explained in "Reference to glacial isostatic adjustment rates" of the main text.

5. Regional tectonic component of VLM: Both Ho Chi Minh City and Rio de Janeiro are at least 800 km away from the nearest major subduction zone and unlikely to experience any significant VLM due to tectonics (see Fig. 2 in the main text). Both are also not located near any other plate tectonic boundaries and can be considered tectonically inactive. We thus assume zero VLM due to regional tectonics.
6. Treatment of relative values of local land subsidence in Ho Chi Minh City: Although there is no available GNSS data to confirm the regional VLM rate, we can assume that there is no expected source of land uplift except from glacial isostatic adjustment[4,5]. Uplift from regional tectonics is unlikely as the city is tectonically inactive. Its selected reference point also resulted in a near-zero maximum (most positive) relative value of local land subsidence as seen in Supplementary A and B. These suggest that its relative land subsidence velocities either do not need to be adjusted or need to be shifted towards the negative so that the velocities will be in a stable reference frame. Therefore, a bathtub model of Ho Chi Minh City using unadjusted relative local land subsidence velocities will represent a conservative estimate of inundated extents.
7. Treatment of relative values of local land subsidence in Rio de Janeiro: There is no expected source of regional land uplift or subsidence due to its tectonically inactive setting and minimal influence from glacial isostatic adjustment[4,5]. Two GNSS records located in areas of around $\pm$1 mm/year of relative local land subsidence also indicate <1 mm/year of VLM (Supplementary B). These suggest that the relative local land subsidence velocities do not need to be shifted by a uniform value. A bathtub model of Rio de Janeiro using unadjusted relative local land subsidence values will likely lead to errors due to this discrepancy of around 1 mm/year.

All data above are projected to the WGS84 EPGS: 4326 geographic coordinates, resampled to the same pixel grid, and cropped to the same spatial extent as the relative local land subsidence velocities. With these data, we compute the bathtub model to estimate areas falling below mean sea-level in 2030 (Table 1). We also subtract a bathtub model without the local land subsidence component from the former bathtub model to estimate additional inundation specifically due to local land subsidence (Fig. 4). The results in both coastal cities show that more land area will be inundated due to local land subsidence (Table 1, Fig. 4).

Table 1: Values used for and results of bathtub models in Ho Chi Minh City and Rio de Janeiro. Positive values refer to land uplift or drop in mean sea-level, and negative values refer to land subsidence or rise in mean sea-level. Abbreviations: mean sea-level (MSL), glacial isostatic adjustment (GIA), relative local land subsidence (RLLS).

| Coastal city | Scenario | MSL change in 2030 (mm) | Present-day GIA rate (mm/year) | Inundation due to MSL change + GIA ($km^2$) | Inundation due to MSL change + GIA + RLLS ($km^2$) | Additional inundation due to RLLS ($km^2$) | Additional % of inundation due to RLLS (%) |
|---|---|---|---|---|---|---|---|
| Ho Chi Minh City | Lower bound | -44.5 | -0.41 | 874.55 | 892.81 | 18.26 | 2.09 |
| | Mean | -91.5 | -0.38 | 878.61 | 898.18 | 19.57 | 2.23 |
| | Upper bound | -159.5 | -0.35 | 884.08 | 904.11 | 20.03 | 2.27 |
| Rio de Janeiro | Lower bound | -57.5 | -0.35 | 11.13 | 12.27 | 1.14 | 10.23 |
| | Mean | -93.5 | -0.31 | 11.53 | 13.47 | 1.94 | 16.82 |
| | Upper bound | -146.5 | -0.28 | 12.08 | 15.60 | 3.52 | 29.13 |

Fig. 4: The additional inundation of land area due to local land subsidence is greater in Ho Chi Minh City (top) than in Rio de Janeiro (bottom). Note that the maps show the mean estimate and the upper and lower bound estimates based on one standard deviation of the rates may be found in the data repository. Abbreviations: mean sea-level (MSL), glacial isostatic adjustment (GIA), relative local land subsidence (RLLS). Administrative boundary: modified from OpenStreetMap. Basemap: ESRI.

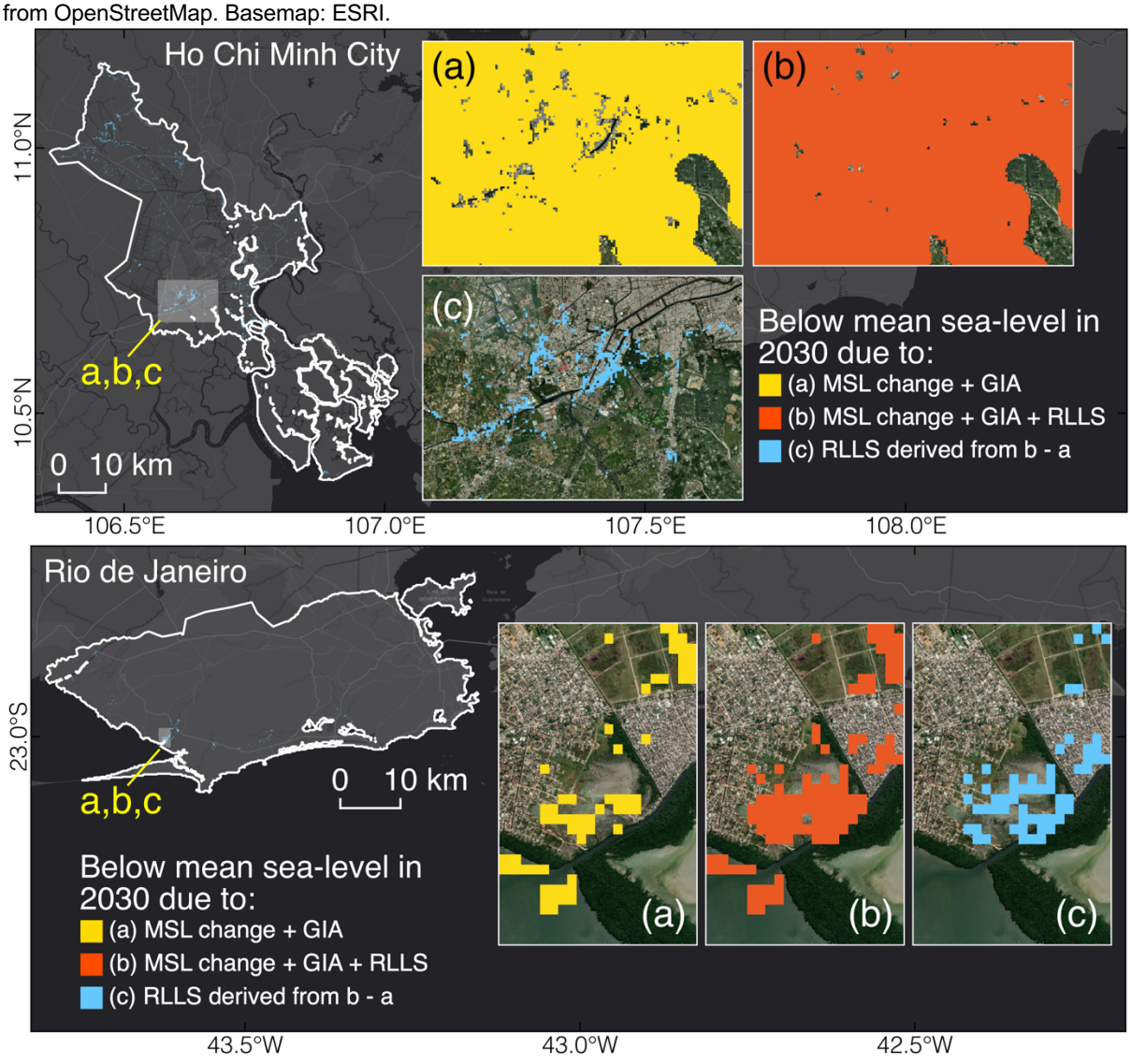

## D. InSAR time series processing

Fig. 5: Effects of InSAR time series processing parameters and corrections. The panels show InSAR line-of-sight velocities over Jakarta (Indonesia) **a.** before phase unwrapping error correction, **b.** after phase unwrapping error correction, **e.** contributed from tropospheric delay correction, **f.** contributed from linear phase deramping, **g.** contributed from topographic residual correction, **c.** after corrections from **e** to **g** are applied, and **d.** identical to **c** but using a random pixel of high coherence for the reference point. The reference point in **a** to **c** was selected through the procedure describe in the Methods. Black crosses indicate the reference point of the velocities. Basemap: ESRI.

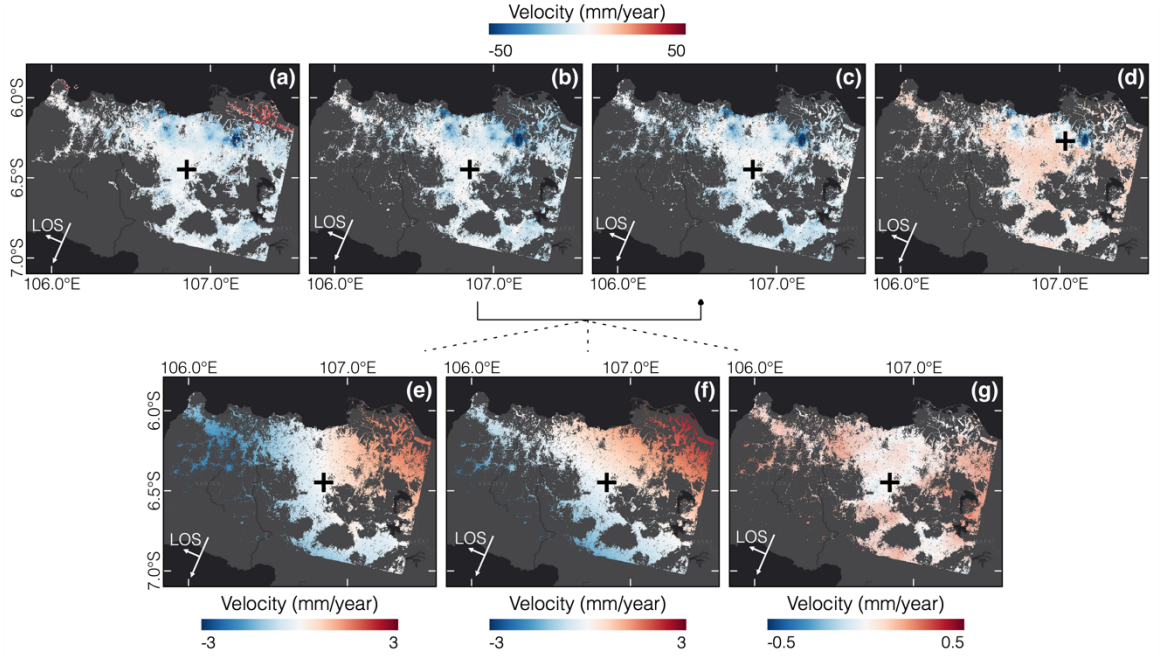

## E. Spatial interpolation of InSAR velocities

Fig. 6: Kriging with variable uncertainties to fill gaps where InSAR velocities could not be derived from time series analysis – an example in Manila (Philippines). The kriged result is more dependent on data points with lower standard deviations. The panels show **a.** velocities and black crosses indicating the locations of quadtree subsampled data points used to estimate kriging parameters, **b, d**. data derived from time series analysis only, and **c, e.** data derived from time series analysis with gaps filled with kriged results. Basemap: ESRI.

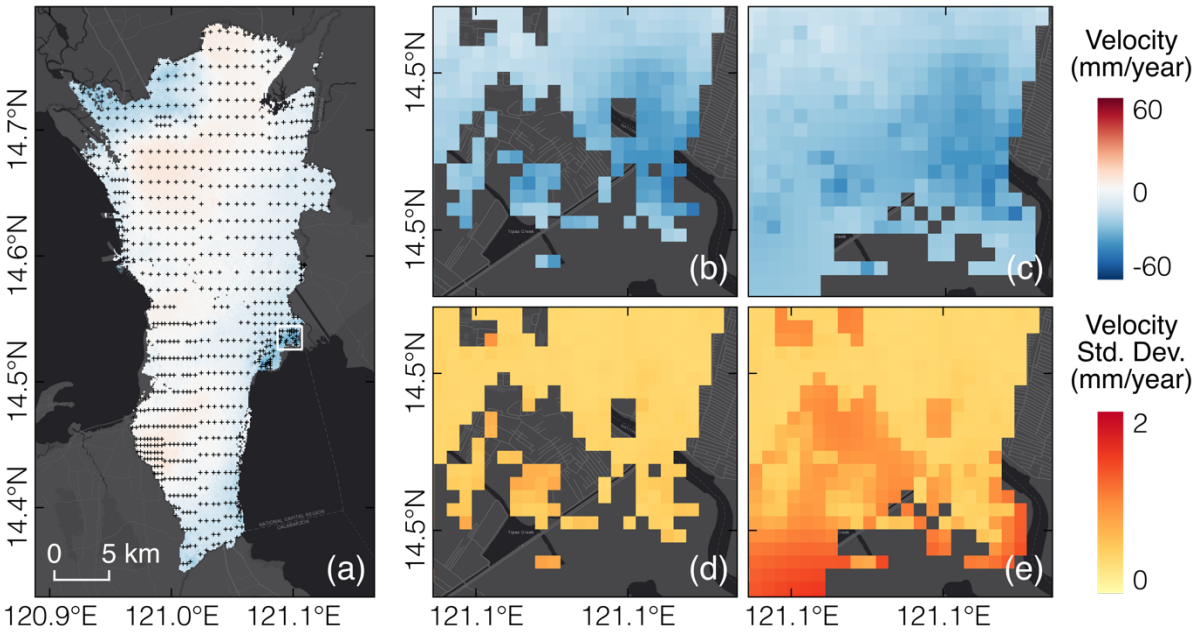

## F. Projection of line-of-sight InSAR velocities to the vertical

We illustrate the difference between velocities projected to the vertical with respect to the ground that are derived from a single look direction and from two look directions. The former refers to using observations from either the ascending or descending orbit, and assuming no horizontal land motion when projecting the line-of-sight observations to the vertical due to a lack of viewing geometry. The latter refers to a combination of observations from both ascending and descending orbits to resolve for vertical and horizontal east-west components, and assuming no horizontal north-south motion due to the satellite's near-polar orbit (Eq. 1 in main text). Any deviation of the projected vertical velocities from the actual vertical velocities increases as horizontal motion increases.

Fig. 7: Comparison of vertical velocities derived from a single look direction and from both look directions combined. The panels show Sentinel-1 InSAR velocities processed within the administrative boundaries of Jakarta (Indonesia) in the **a.** vertical direction from an ascending orbit, **b.** vertical direction from a descending orbit, **c.** vertical direction from a combination of both look directions, and **d.** horizontal east-west direction from a combination of both look directions. Black crosses indicate the reference point of the velocities, thick white arrow indicates the fastest subsiding area. Basemap: ESRI.

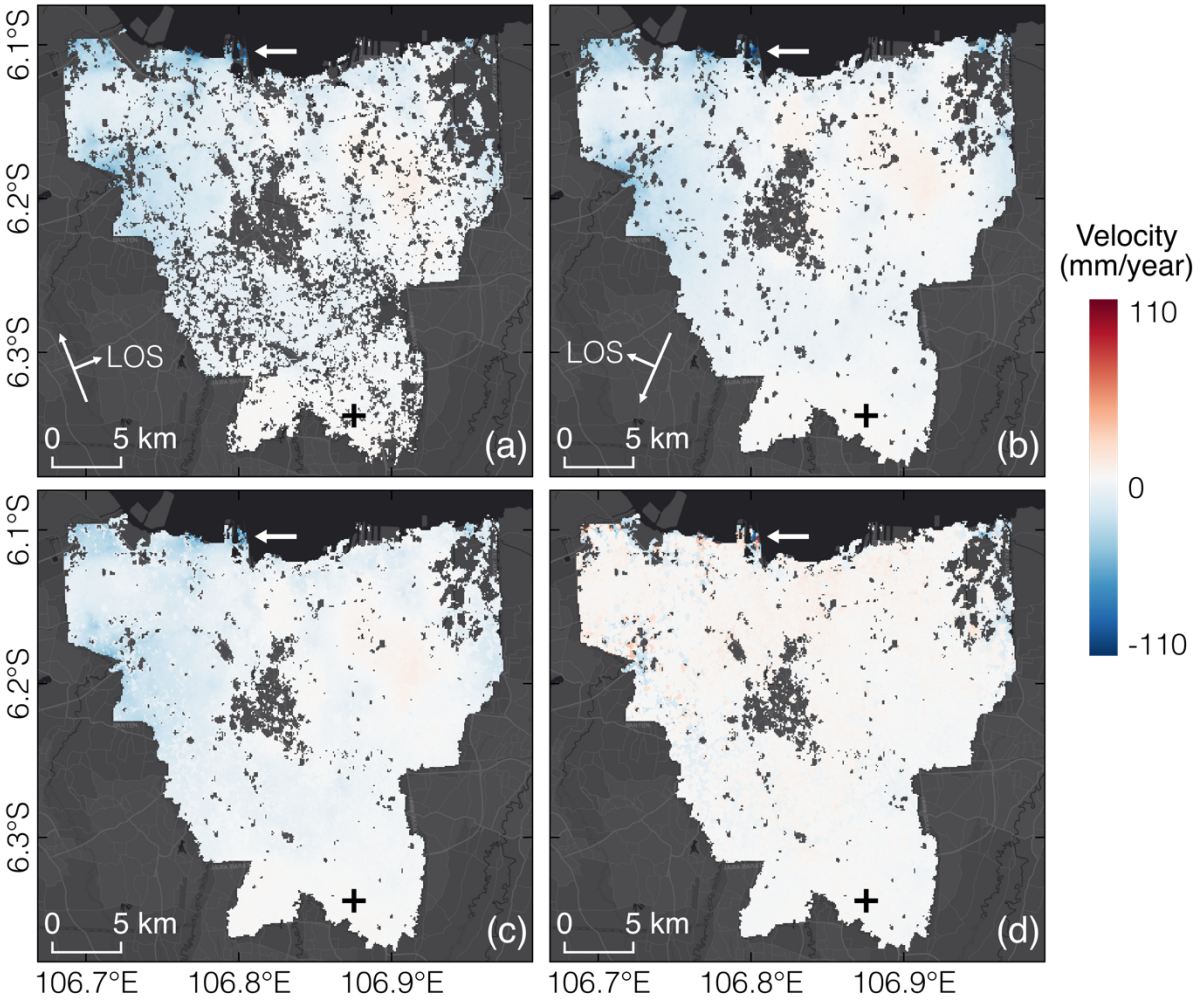


We show an example in Jakarta (Indonesia), where some horizontal land motion may be expected to accompany large vertical land motion due to the presence of rapidly subsiding areas (Fig. 7). It should be noted that the ascending orbit velocities are noisier and have fewer coherent pixels than that of the descending orbit, likely due to noise from tropospheric delay.

The vertical velocities are overall similar across the single-look ascending, single-look descending and double-look cases. At the center of the fastest subsiding area, the single-look ascending, single-look descending, double-look vertical and double-look horizontal east-west velocities are -92 mm/year, -103 mm/year, -94 mm/year and -11 mm/year respectively. Horizontal land motion is still significantly smaller than vertical land motion in the fastest subsiding areas. Thus, InSAR observations from a single look direction were used in this study to produce relative local land subsidence rates for a large number of coastal cities worldwide for practical reasons.

## G. Summary of velocities

Table 2: Statistics of velocities of different components of relative sea-level. Percentiles indicate the spatial variation in velocities that can be found within a coastal city and are denoted 'p'. For example, 16$^{th}$ percentile is denoted p16. Positive values refer to land uplift or drop in mean sea-level, and negative values refer to land subsidence or rise in mean sea-level.

| # | Coastal city | Country | InSAR-derived relative local land subsidence (mm/year) | | | | ICE-6G_C (VM5a) glacial isostatic adjustment (mm/year) | | | IPCC AR6 vertical land motion (mm/year) | | | IPCC AR6 climate-driven mean sea-level change (mm/year) | | |
|---|---|---|---|---|---|---|---|---|---|---|---|---|---|---|---|
| | | | p16 | p50 | p84 | p95 of negative velocities | p16 | p50 | p84 | p16 | p50 | p84 | p16 | p50 | p84 |
| 1 | Abidjan | Côte d'Ivoire | -6.8 | -1.9 | 3.4 | -11.6 | -0.2 | -0.1 | -0.1 | 0.2 | 0.3 | 0.3 | -4.7 | -4.7 | -4.7 |
| 2 | Ahmedabad | India | -13.6 | -4.7 | -0.4 | -22.7 | 0.4 | 0.4 | 0.4 | 0.4 | 0.4 | 0.4 | -3.8 | -3.8 | -3.7 |
| 3 | Alexandria | Egypt | -2.7 | 0.0 | 2.8 | -7.4 | -0.1 | -0.1 | 0.0 | -0.5 | 0.0 | 0.2 | -4.4 | -4.4 | -4.4 |
| 4 | Bangkok | Thailand | -3.1 | 0.0 | 2.2 | -7.0 | 0.3 | 0.3 | 0.4 | -6.2 | 0.4 | 0.4 | -4.0 | -3.9 | -3.9 |
| 5 | Barcelona | Spain | -4.8 | -0.6 | 0.9 | -10.8 | -0.5 | -0.4 | -0.2 | -0.8 | -0.3 | 0.1 | -4.3 | -4.3 | -4.3 |
| 6 | Buenos Aires | Argentina | -1.3 | -0.3 | 0.5 | -3.7 | 0.6 | 0.6 | 0.7 | 0.0 | 0.0 | 0.0 | -3.5 | -3.5 | -3.5 |
| 7 | Chennai | India | -2.6 | 0.4 | 2.1 | -11.3 | 0.2 | 0.2 | 0.2 | 0.2 | 0.3 | 0.8 | -4.0 | -3.9 | -3.9 |
| 8 | Chittagong | Bangladesh | -27.1 | -11.8 | -0.7 | -37.4 | 0.3 | 0.4 | 0.4 | -0.6 | 0.4 | 0.6 | -3.6 | -3.6 | -3.5 |
| 9 | Dalian | China | -3.8 | -0.1 | 3.0 | -9.3 | 0.4 | 0.4 | 0.5 | 0.3 | 0.4 | 0.4 | -4.4 | -4.3 | -4.3 |
| 10 | Dar es Salaam | Tanzania | -2.5 | -0.5 | 1.0 | -5.0 | -0.2 | -0.1 | -0.1 | 0.1 | 0.2 | 0.3 | -4.9 | -4.9 | -4.9 |
| 11 | Dhaka | Bangladesh | -4.1 | -0.3 | 2.3 | -12.0 | 0.4 | 0.4 | 0.4 | 0.4 | 0.4 | 0.4 | -3.5 | -3.5 | -3.5 |
| 12 | Dongguan | China | -1.7 | -0.1 | 1.5 | -5.1 | 0.5 | 0.5 | 0.5 | 0.4 | 0.4 | 0.4 | -4.3 | -4.3 | -4.3 |
| 13 | Foshan | China | -5.6 | -1.7 | 0.6 | -10.7 | 0.5 | 0.5 | 0.5 | 0.4 | 0.4 | 0.4 | -4.3 | -4.3 | -4.3 |
| 14 | Fukuoka | Japan | -8.6 | -2.8 | 0.8 | -12.5 | 0.5 | 0.5 | 0.5 | -0.1 | -0.1 | -0.1 | -4.6 | -4.6 | -4.6 |
| 15 | Guangzhou | China | -6.3 | -1.9 | 1.5 | -13.6 | 0.5 | 0.5 | 0.5 | 0.3 | 0.4 | 1.0 | -4.3 | -4.3 | -4.3 |
| 16 | Hangzhou | China | -3.8 | -0.9 | 1.9 | -7.0 | 0.5 | 0.5 | 0.5 | 0.5 | 0.5 | 0.5 | -4.5 | -4.4 | -4.4 |
| 17 | Ho Chi Minh City | Vietnam | -31.7 | -16.2 | -3.2 | -42.7 | 0.4 | 0.4 | 0.4 | 0.2 | 0.5 | 0.5 | -4.1 | -4.1 | -4.0 |
| 18 | Hong Kong | China | -5.5 | -1.1 | 1.4 | -13.0 | 0.4 | 0.4 | 0.4 | -0.8 | 0.3 | 1.4 | -4.3 | -4.3 | -4.3 |
| 19 | Houston | USA | -10.2 | -2.8 | 1.6 | -17.3 | -0.8 | -0.8 | -0.8 | -6.3 | -5.0 | -2.3 | -5.0 | -5.0 | -5.0 |
| 20 | Istanbul | Turkey | -12.2 | -6.2 | -0.6 | -19.4 | -0.1 | -0.1 | 0.0 | -0.1 | 0.1 | 0.1 | -3.5 | -3.5 | -3.3 |
| 21 | Jakarta | Indonesia | -14.0 | -4.4 | 0.2 | -26.1 | 0.0 | 0.0 | 0.1 | 0.3 | 0.3 | 0.4 | -3.7 | -3.7 | -3.7 |
| 22 | Karachi | Pakistan | -3.1 | -0.2 | 2.1 | -6.2 | 0.3 | 0.3 | 0.4 | -0.2 | -0.2 | -0.2 | -3.9 | -3.9 | -3.7 |

| | | | | | | | | | | | | | | | |
|---|---|---|---|---|---|---|---|---|---|---|---|---|---|---|---|
| 23 | Kolkata | India | -5.2 | -1.9 | 0.4 | -8.3 | 0.4 | 0.4 | 0.4 | 4.9 | 4.9 | 4.9 | -3.5 | -3.5 | -3.5 |
| 24 | Lagos | Nigeria | -7.0 | -1.4 | 3.1 | -17.2 | -0.2 | -0.2 | -0.2 | 0.1 | 0.2 | 0.2 | -4.7 | -4.6 | -4.6 |
| 25 | Lima | Peru | -2.3 | -0.6 | 0.7 | -4.4 | 0.1 | 0.1 | 0.1 | 1.1 | 1.1 | 1.1 | -4.1 | -4.0 | -4.0 |
| 26 | London | England | -4.0 | -0.3 | 2.5 | -8.8 | -0.4 | -0.4 | -0.4 | -0.2 | -0.1 | 0.2 | -4.3 | -4.3 | -4.2 |
| 27 | Los Angeles | USA | -2.7 | -0.7 | 0.9 | -4.6 | -0.7 | -0.7 | -0.7 | -0.2 | 0.1 | 0.3 | -3.7 | -3.6 | -3.5 |
| 28 | Luanda | Angola | -2.2 | 0.6 | 4.2 | -7.6 | -0.2 | -0.2 | -0.1 | 0.1 | 0.1 | 0.2 | -4.8 | -4.7 | -4.7 |
| 29 | Manila | Philippines | -8.8 | -1.7 | 2.3 | -17.0 | 0.4 | 0.4 | 0.4 | -5.5 | -5.2 | -5.0 | -3.8 | -3.8 | -3.7 |
| 30 | Miami | USA | -2.1 | -0.1 | 1.6 | -4.5 | -0.9 | -0.8 | -0.8 | -1.1 | -1.0 | -0.8 | -4.9 | -4.8 | -4.7 |
| 31 | Mumbai | India | -3.9 | -0.9 | 1.5 | -8.9 | 0.3 | 0.3 | 0.4 | 0.5 | 0.5 | 0.5 | -4.1 | -4.0 | -4.0 |
| 32 | Nagoya | Japan | -0.6 | 0.2 | 0.9 | -2.4 | 0.5 | 0.5 | 0.5 | -1.5 | 0.5 | 3.1 | -4.7 | -4.7 | -4.7 |
| 33 | Nanjing | China | -4.0 | 1.1 | 5.4 | -8.2 | 0.4 | 0.4 | 0.4 | 0.5 | 0.5 | 0.5 | -4.5 | -4.5 | -4.3 |
| 34 | New York | USA | -1.8 | -0.6 | 0.3 | -3.9 | -1.8 | -1.8 | -1.8 | -1.3 | -1.3 | -1.3 | -6.0 | -5.8 | -5.7 |
| 35 | Osaka | Japan | -4.1 | -1.7 | 0.4 | -6.2 | 0.5 | 0.5 | 0.5 | -3.0 | -3.0 | -3.0 | -4.7 | -4.7 | -4.7 |
| 36 | Philadelphia | USA | -1.6 | -0.2 | 1.1 | -4.3 | -2.0 | -2.0 | -2.0 | -1.5 | -1.5 | -1.5 | -5.9 | -5.9 | -5.9 |
| 37 | Qingdao | China | -6.4 | -3.6 | -0.4 | -9.8 | 0.4 | 0.4 | 0.5 | 0.3 | 0.3 | 0.3 | -4.4 | -4.3 | -4.2 |
| 38 | Rio de Janeiro | Brazil | -4.3 | -2.4 | -1.2 | -6.9 | 0.3 | 0.3 | 0.3 | -0.2 | 0.1 | 0.2 | -4.2 | -4.2 | -4.1 |
| 39 | Saint Petersburg | Russia | -3.5 | -1.7 | -0.2 | -5.7 | 1.6 | 1.7 | 1.8 | 0.4 | 1.0 | 1.7 | -6.8 | -6.1 | -5.3 |
| 40 | Seoul | South Korea | -1.3 | -0.2 | 0.9 | -3.3 | 0.6 | 0.6 | 0.6 | 0.4 | 0.4 | 0.6 | -4.6 | -4.6 | -4.5 |
| 41 | Shanghai | China | -7.3 | -2.5 | 1.1 | -14.1 | 0.5 | 0.6 | 0.6 | 0.5 | 0.5 | 0.5 | -4.5 | -4.5 | -4.4 |
| 42 | Singapore | Singapore | -4.0 | -1.4 | 0.5 | -6.9 | 0.1 | 0.2 | 0.2 | 0.4 | 0.5 | 1.2 | -4.0 | -4.0 | -4.0 |
| 43 | Surat | India | -9.5 | -4.7 | -0.5 | -16.5 | 0.4 | 0.4 | 0.4 | -0.3 | 0.4 | 0.4 | -3.8 | -3.8 | -3.7 |
| 44 | Suzhou | China | -7.2 | -1.4 | 3.6 | -13.2 | 0.5 | 0.5 | 0.5 | 0.4 | 0.5 | 0.5 | -4.5 | -4.5 | -4.5 |
| 45 | Tianjin | China | -20.9 | -5.7 | 4.2 | -42.9 | 0.4 | 0.4 | 0.4 | 0.1 | 0.3 | 0.4 | -4.2 | -4.2 | -4.1 |
| 46 | Tokyo | Japan | -1.6 | -0.7 | 0.6 | -2.7 | 0.5 | 0.5 | 0.5 | -0.3 | 0.8 | 1.9 | -4.8 | -4.7 | -4.7 |
| 47 | Washington, D.C. | USA | -0.6 | 0.6 | 1.9 | -2.6 | -1.7 | -1.7 | -1.7 | -1.7 | -1.7 | -1.7 | -6.0 | -6.0 | -5.9 |
| 48 | Yangon | Myanmar | -13.3 | -3.9 | 2.1 | -30.8 | 0.4 | 0.4 | 0.4 | -1.8 | -1.8 | -1.8 | -3.7 | -3.6 | -3.5 |

## References


1. Fox-Kemper, B. et al. Climate Change 2021: The Physical Science Basis. Contribution of Working Group I to the Sixth Assessment Report of the Intergovernmental Panel on Climate Change [Masson-Delmotte, V., Zhai, P., Pirani, A., Connors, S. L., Péan, C., Berger, S., Caud, N., Chen, Y., Goldfarb, L., Gomis, M. I., Huang, M., Leitzell, K., Lonnoy, E., Matthews, J. B. R., Maycock, T. K., Waterfield, T., Yelekçi, O., Yu, R. and Zhou B.]. (Cambridge University Press, In press).
2. Garner, G. G. et al. Framework for Assessing Changes To Sea-level (FACTS). Geoscientific Model Development (in prep).
3. Garner, G. G. et al. IPCC AR6 Sea-Level Rise Projections. Version 20210809.
4. Peltier, W. R., Argus, D. & Drummond, R. Space geodesy constrains ice age terminal deglaciation: The global ICE-6G_C (VM5a) model. J. Geophys. Res. Solid Earth **120**, 450–487 (2015).
5. Argus, D. F., Peltier, W., Drummond, R. & Moore, A. W. The Antarctica component of postglacial rebound model ICE-6G_C (VM5a) based on GPS positioning, exposure age dating of ice thicknesses, and relative sea level histories. Geophys. J. Int. **198**, 537–563 (2014).
6. Shirzaei, M. et al. Measuring, modelling and projecting coastal land subsidence. Nat. Rev. Earth Environ. **2**, 40–58 (2021).
7. Kulp, S. A. & Strauss, B. H. CoastalDEM: a global coastal digital elevation model improved from SRTM using a neural network. Remote Sens. Environ. **206**, 231–239 (2018).
8. NASA JPL. NASA Shuttle Radar Topography Mission Global 1 arc second. (2013) doi:10.5067/MEASURES/SRTM/SRTMGL1.003.
9. Li, T. et al. Uncertainties of glacial isostatic adjustment model predictions in North America associated with 3D structure. Geophys. Res. Lett. **47**, e2020GL087944 (2020).